A Robust and Efficient Propane Dehydrogenation Catalyst from Unexpectedly Segregated Pt₂Mn Nanoparticles

Lukas Rochlitz, Quentin Pessemesse, Jörg W. A. Fischer, Daniel Klose, Adam H. Clark, Milivoj Plodinec, Gunnar Jeschke, Pierre-Adrien Payard,* and Christophe Copéret*

ABSTRACT: The increasing demand for short chain olefins like propene for plastics production and the availability of shale gas make the development of highly performing propane dehydrogenation (PDH) catalysts, robust toward industrially applied harsh regeneration conditions, a highly important field of research. A combination of surface organometallic chemistry and thermolytic molecular precursor approach was used to prepare a nanometric, bimetallic Pt−Mn material (3 wt % Pt, 1.3 wt % Mn) supported on silica *via* consecutive grafting of a Mn and Pt precursor on surface OH groups present on the support surface, followed by a treatment under a H₂ flow at high temperature. The material exhibits a 70% fraction of the overall Mn as Mn^{II} single sites on the support surface; the remaining Mn is incorporated in segregated Pt₂Mn nanoparticles. The material shows great performance in PDH reaction with a low deactivation rate. In particular, it shows outstanding robustness during repeated regeneration cycles, with conversion and selectivity stabilizing at *ca.* 37 and 98%, respectively. Notably, a material with a lower Pt loading of only 0.05 wt % shows an outstanding catalytic performance—initial productivity of 4523 $g_{C_3H_6}/g_{Pt}$ h and an extremely low k_d of 0.003 h^{-1} under a partial pressure of H₂, which are among the highest reported productivities. A combined *in situ* X-ray absorption spectroscopy, scanning transmission electron microscopy, electron paramagnetic resonance, and metadynamics at the density functional theory level study could show that the strong interaction between the Mn^{II}-decorated support and the unexpectedly segregated Pt₂Mn particles is most likely responsible for the outstanding performance of the investigated materials.
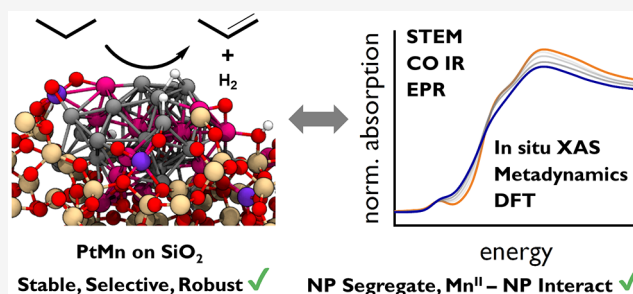
1. INTRODUCTION

Some of the most important classes of heterogeneous catalysts are based on bimetallic systems, as they facilitate numerous selective transformations, some of them being operated on a megaton scale in the petrochemical industry and enabling for instance the production of short-chain olefins as building blocks for polymers and bulk chemicals.[1] In that context, non-oxidative propane dehydrogenation (PDH) has gained renewed interest in recent years as an alternative propene production route due to a rising propene demand and its current, decreasing production *via* classical cracking routes as a result of changes in refinery technology.[1−4] The Oleflex process, based on an alumina-supported Pt−Sn system, was one of the first industrially implemented catalysts for PDH in the 1990s to produce propene.[1] Since then, Pt-based bi- and multi-metallic materials have been among the most investigated systems for this transformation. The general drawback of PDH is its highly endothermic nature (ΔH^0_{298} = 124.3 kJ mol^{-1}); this thermodynamic limitation requires high reaction temperatures (550−750 °C) to reach reasonable conversion levels. Such harsh reaction conditions favor sintering of the catalytically active phase and coke formation

via hydrocarbon cracking even for advanced, multi-metallic materials. Both events lead to catalyst deactivation which is combated by constant regeneration cycles.[1,4,5] Some regeneration strategies involve short PDH cycles followed by short flow of different gasses—oxidation in air (Pt dispersion and coke removal; sometimes oxychlorination to improve Pt dispersion) and reduction with H₂ (reactivation of the active phase)—which is repeated over years.[4] Therefore, the search for catalysts exhibiting high catalytic performances, combined with robustness toward repeated regeneration cycles, is of major importance for further improving PDH catalysts.

In order to find suitable materials, research efforts have concentrated on the use of post transition metal or main group element promoters like Zn,[6−13] B,[14,15] Ga,[16−20] In,[21−23] and Sn[1,5,24] in combination with varying supports. All these
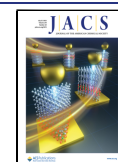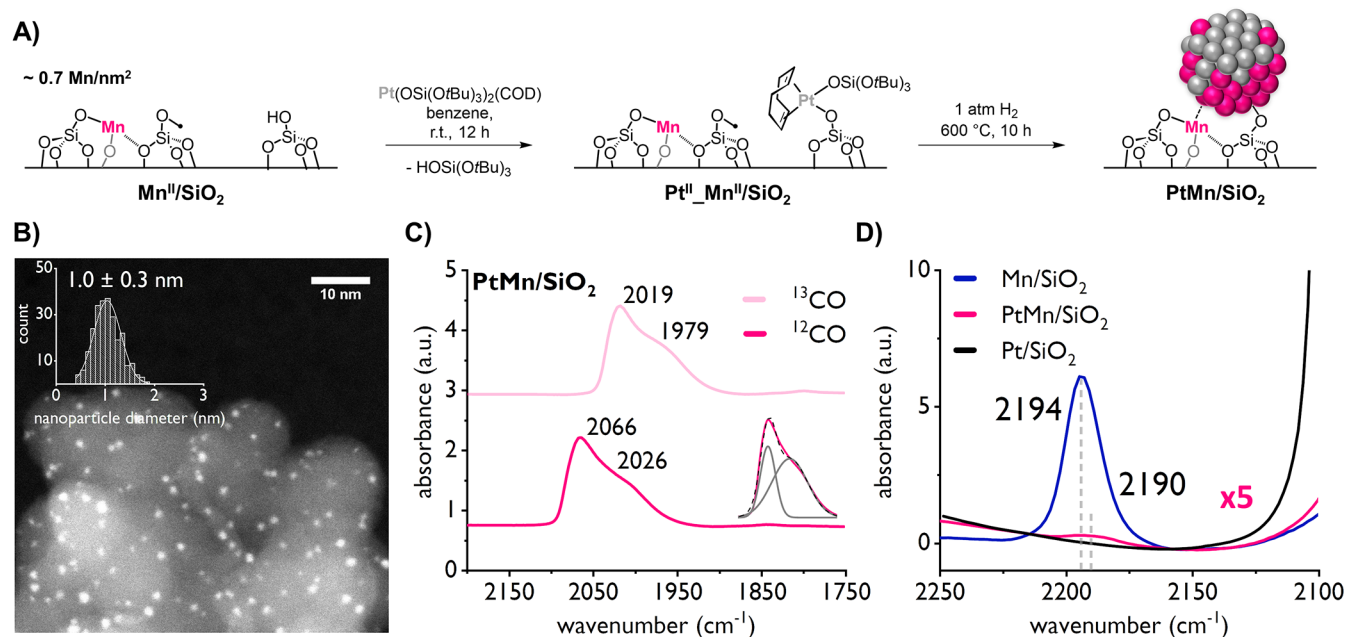
Figure 1. (A) Synthetic approach for PtMn/SiO$_2$ resulting in segregated Pt$_2$Mn nanoparticles in strong interaction with Mn^{II} sites at the support surface. (B) Representative STEM micrograph of PtMn/SiO$_2$ and corresponding particle size distribution (PSD) (inset). (C) Background-subtracted FTIR spectra of adsorbed ^{12}CO and ^{13}CO on PtMn/SiO$_2$; insert shows fitting of the two bands for ^{12}CO. (D) ^{12}CO adsorption FTIR spectra of Mn^{II}/SiO$_2$, Pt/SiO$_2$, and PtMn/SiO$_2$ showing the area of expected adsorption on Lewis acidic sites; note that the spectra are normalized to the Si−O bending vibrational frequency around 1865 cm^{-1} to allow for intensity comparison. The PtMn/SiO$_2$ intensity needed to be increased 5 fold for better visibility, indicating minor adsorption of CO molecules on PtMn/SiO$_2$ compared to Mn^{II}/SiO$_2$.

promoters are known to drastically increase the PDH performance compared to monometallic Pt by increasing both selectivity and stability. All of these promoters have been heavily investigated, and the corresponding materials were analyzed and characterized in great detail. While In and Zn are not utilized in industries, Sn and, more recently, Ga promoters are both already applied in industrial processes.[17,25] The promoters can fulfill several roles: (i) neutralization of the support acidity that usually leads to cracking side reactions, (ii) suppression of metal sintering, and (iii) minimization of cracking by avoiding deep hydrogenolysis and by easing desorption of the olefinic product due to alloy formation of Pt with the promoter element (site isolation). Besides these classical promoter elements, there are significantly fewer reports regarding the use of transition-metal elements as promoters for PDH. While early 3d transition metals usually do not easily form alloyed phases with Pt and are therefore probably not suitable as PDH catalysts, later transition metals can offer possible alternatives; a noteworthy reported example is Pt−Mn, which displays promising catalytic performance in PDH.[26,27] These improved catalytic performances have been proposed to be related to the formation of different active phases, from Pt/Pt$_3$Mn core/shell structured nanoparticles to well-defined Pt$_3$Mn and PtMn$_3$ alloys as well as Pt$_x$Mn$_y$ with different Pt−Mn ratios.

Our group has recently introduced a methodology based on surface organometallic chemistry (SOMC)[28−31] and thermolytic molecular precursor (TMP)[32] approaches to generate bimetallic systems with tailored interfaces and compositions.[33,34] In these systems, SiO$_2$ was preferentially used because it is a high-surface-area, non-reducible, thermally stable support with no Lewis and low Brønsted acidity and no strong metal−support interaction. SiO$_2$ is thus ideally suited to

study structure−property relationships of surface species, avoiding interference from the support. This SOMC/TMP approach combined with detailed spectroscopic—including X-ray absorption spectroscopy (XAS), X-ray photoelectron spectroscopy (XPS), and infrared spectroscopy (IR)—and computational studies—using in particular metadynamics (MTD) at the density-functional theory (DFT) level[35]—has enabled the development of PtGa-based PDH catalysts with high catalytic performances. Such analysis helped to derive structure−performance relationships, tracing back the catalytic performance to (i) Pt site isolation at the nanoparticle surface and (ii) increased dynamics of Pt sites in the alloyed nanoparticles. While Ga itself exhibits catalytic activity in the PDH reaction,[36−38] we proposed that its main role in the PtGa system is the improvement of the stability of PtGa alloyed nanoparticles due to strong interaction with Ga^{III} surface sites.[35] Considering the promising catalytic performances of recently reported PtMn systems discussed above and the need to constantly improve our understanding of PDH catalysts, we here explored the generation of tailored PtMn bimetallic systems using the SOMC/TMP approach in combination with MTD at the DFT level. First, we determined the composition of such particles via X-ray absorption near edge structure (XANES) and elemental analysis (EA). In a second step, we utilize these data to develop a simple model based on exploration of possible structures of PtMn nanoparticles by MTD. Such a model proved useful to detect spatial separation of Pt and Mn inside the particle and to explain experimental CO adsorption Fourier-transform infrared spectroscopy (FTIR) results. In order to refine the structure derived from experimental extended X-ray absorption fine structure (EXAFS), we further improve this simple model by incorporating the support, which improved the fit between

computationally and experimentally derived coordination numbers (CNs).

In detail, using a combined experimental—including CO adsorption FTIR, high-angle annular dark-field scanning transmission electron microscopy (HAADF-STEM), and XAS among others—and computational approach, we were able to develop a robust PtMn PDH catalyst (PtMn/SiO$_2$, 2.97 wt % Pt, 1.34 wt % Mn), based on Pt$_2$Mn nanoparticles supported on Mn^{II}-doped silica. Decreasing Pt loading from 3.0 to 0.05 wt % (Pt(0.05)Mn/SiO$_2$, 1.38 wt % Mn) drastically improved the productivity; co-feeding H$_2$ additionally further increased the stability compared to the higher Pt loading material. Finally, consecutive fast regeneration cycles on the high loading PtMn catalyst revealed great robustness and unchanged high selectivity. The detailed spectroscopic investigations augmented with MTD on the high Pt-loading catalyst reveal that this silica-supported PtMn material is based on segregated Pt$_2$Mn nanoparticles where reduced Mn accumulates at the interface between the Pt rich inner part of the particles and the oxide surface, interacting with additional Mn^{II} sites present at the silica support surface.

2. RESULTS AND DISCUSSION

We first prepared the silica-supported Pt—Mn material *via* a two-step SOMC/TMP process (Figure 1A)[6,16] from highly dispersed Mn sites on SiO$_2$.[39] The Mn single sites, Mn^{II}/SiO$_2$, prepared *via* SOMC from [Mn(OSi(OtBu)$_3$)$_2$]$_2$ and SiO$_{2-700}$ (see the Supporting Information for experimental details) contain Mn^{II} sites (0.73 Mn/nm^2, 1.37 wt % Mn) free of organic ligands along with isolated surface OH groups (*ca.* 1 OH/nm^2).[39] Then, Pt was introduced by grafting [Pt(OSi(OtBu)$_3$)$_2$(COD)] (0.26 mmol Pt/g SiO$_2$)[40,41] (COD = 1,5-cyclooctadiene) onto the surface OH groups of Mn^{II}/SiO$_2$, yielding a material—Pt^{II}_Mn^{II}/SiO$_2$—that was then submitted to a flow of H$_2$ at 600 °C leading to the formation of PtMn/SiO$_2$. The final material is obtained as a black solid (2.97 wt % Pt and 1.34 wt % Mn; 1:1.6 (Pt:Mn/mol:mol)), indicating particle formation.

HAADF-STEM images of PtMn/SiO$_2$ evidence the formation of narrowly distributed and well-dispersed, nano-sized particles (1.0 ± 0.3 nm) along with smaller clusters as well as a small minority of single Pt atoms on the support surface (Figure 1B and Supporting Information Figure S5). Note that a monometallic Pt/SiO$_2$ material, prepared *via* the same approach, shows considerably larger particles and broader PSD of 2.0 ± 0.8 nm, already indicating a significant effect of Mn on the nanoparticle structure (Supporting Information Figure S2). To obtain information about the surface state of these nanoparticles, FTIR spectra of a PtMn/SiO$_2$ pellet exposed to ^{12}CO and ^{13}CO (around 10 mg, 120 mbar) were recorded. The subtraction of a spectrum acquired after exposure to ^{12}CO shows two major vibrational bands centered at 2066 and 2026 cm^{-1} along with a very weak band around 1844 cm^{-1} (Figure 1C, Supporting Information Figures S14 and S15). The two bands at higher wavenumbers are red-shifted by 18 and 65 cm^{-1} compared to monometallic Pt particles supported on SiO$_2$ (2084 cm^{-1}, Figure S12), indicating a clear change of the electronic structure of Pt. Additionally, the existence of two vibrational bands indicates more than one CO adsorption site on the particle surface. An additional vibrational band around 1844 cm^{-1} of weak intensity can be assigned to μ_2 bridging ^{12}CO on adjacent Pt atoms. Furthermore, another weak vibrational band around

2190 cm^{-1} (Figure 1D) is observed and can be associated with CO being adsorbed on residual Mn^{II} sites; Mn^{II}/SiO$_2$ contacted with CO shows a band at 2194 cm^{-1} (Figure 1D, Supporting Information Figure S13). Comparing the intensities of the features (2190 and 2194 cm^{-1}), it can be concluded that in PtMn/SiO$_2$, only a small amount of Mn^{II} sites dispersed at the support surface exists while the majority of Mn in the sample consists of either Mn as part of the nanoparticles or Mn^{II} sites at the support interface with the nanoparticles (*vide infra*), therefore not being accessible for CO adsorption. Equivalently recorded ^{13}CO adsorption spectra show a consistent red shift of around 45 cm^{-1}, in agreement with all observed vibrational frequencies resulting from adsorbed CO.

We also performed H$_2$ and CO chemisorption studies showing very similar Q_{sat} values for PtMn/SiO$_2$ (2.6 mmol CO/g$_{Pt}$, 1.6 mmol H$_2$/g$_{Pt}$) and Pt/SiO$_2$ (2.5 mmol CO/g$_{Pt}$, 1.7 mmol H$_2$/g$_{Pt}$) which underlines that there must be an inherent difference in the nanoparticle structure in the two systems given the particle size difference of the two materials (1 nm for PtMn/SiO$_2$ and 2 nm for Pt/SiO$_2$) (Figures S16 and S17 and Table S1). XPS spectra of the 2p binding energy region of Mn for Mn^{II}/SiO$_2$ and PtMn/SiO$_2$ show features at similar binding energies, while differences in the line shape are observed as broader and more asymmetric for the bimetallic material, which could be indicative of an additional lower energy feature associated to partial reduction of Mn. For the Pt 4f$_{7/2}$ binding energy, a small shift of −0.2 eV is observed, going from Pt/SiO$_2$ to PtMn/SiO$_2$ accompanied by a line broadening, which could be attributed to a particle size effect as well as Pt—Mn interaction or alloy formation.[42,43] (see Supporting Information Figures S18 and S19 for detail).

To further analyze the composition and structure of the PtMn particles as well as the chemical state of Pt and Mn on the SiO$_2$ support, we performed an XAS study in combination with MTD calculations at the DFT level on model systems to refine the structure. First we carried out an *in situ* XANES analysis of Pt^{II}_Mn^{II}/SiO$_2$ at both, the Mn K and Pt L$_{III}$-edge under a flow of H$_2$ from room temperature to 600 °C (see Supporting Information for detail). The results are depicted in Figure 2A. As seen from the Mn K edge spectra, the material before (Pt^{II}_Mn^{II}/SiO$_2$, blue, 6546.0 eV) and after (PtMn/SiO$_2$, pink, 6545.6 eV) temperature-programmed reduction (TPR, increase of T from RT to 600 °C under a flow of H$_2$) shows a small change in the rising edge feature, indicating partial reduction of Mn^{II} sites.

A linear combination fit (LCF) (Figures S23 and S24) of the spectrum after TPR points to a partial reduction of Mn^{II} to Mn^0 by roughly 30% of the total Mn (Table 1). In contrast, analysis at the Pt L$_{III}$ edge indicates full Pt reduction after TPR (Figure 2A) under the assumption that the small differences and edge energy shift from 11,564.0 to 11,564.3 eV compared to Pt foil can be attributed to Pt—Mn interaction and/or a particle size effect.[44] Combination of the data of reduced Pt (100%) and Mn (30%) with EA results, allows us to evaluate the average ratio of reduced Pt and Mn in the nanoparticles—which is close to 2:1 (Pt—Mn) for Pt^{II}_Mn^{II}/SiO$_2$ after TPR (Table 1). Hence, the data indicate the formation of nanoparticles with an average composition close to Pt$_2$Mn in PtMn/SiO$_2$ (EXAFS and Figure 2B will be discussed only later; *vide infra*).

To further track the evolution of Mn in these samples as indicated by the LCF XANES analysis at the Mn K edge, we
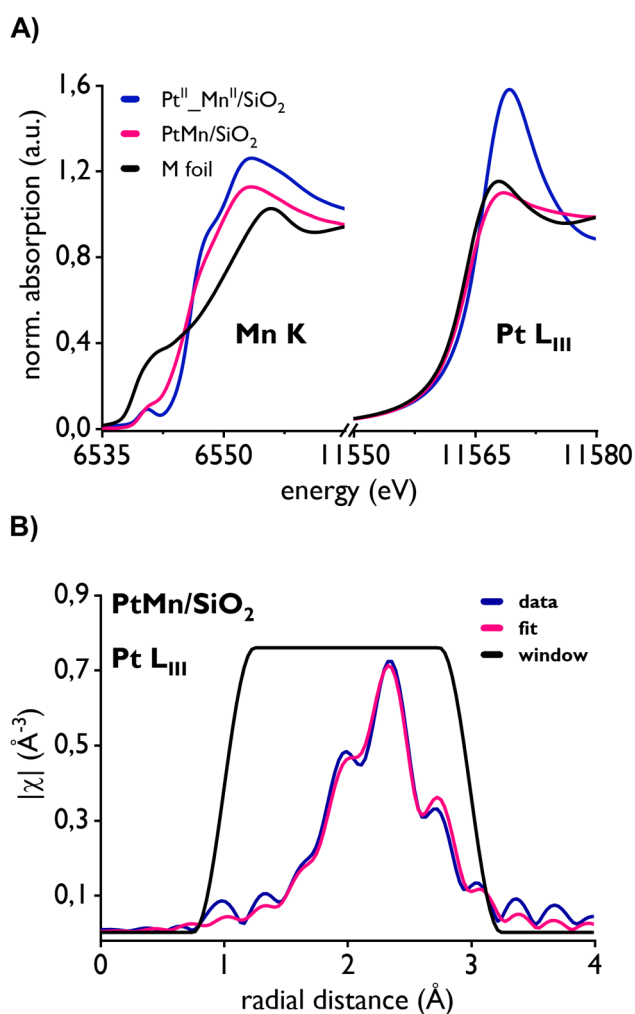
Figure 2. (A) XANES spectra of $PtMn/SiO_2$ after treatment under H_2 (pink) at the Mn K and Pt L_{III} edge and corresponding reference spectra (blue and black), indicating partial reduction of Mn and full reduction of Pt. (B) EXAFS fit of $PtMn/SiO_2$ at the Pt L_{III} edge with good agreement of data and fit.

dipole−dipole broadening for these $S = 5/2$ species,[45] exchange coupling between the sites, and ^{55}Mn hyperfine coupling are all expected to be of similar magnitude. Moreover, exchange coupling and dipole−dipole coupling are distributed. In this situation, one may expect loss of the Mn hyperfine resolution for the $m_S = −1/2 \leftrightarrow m_S = +1/2$ transitions, as we observe in the spectra. Large zero-field splitting and a broad distribution of zero-field splitting due to variations in molecular geometry of the surface species may further compound such broadening. The spectral differences between Mn^{II}/SiO_2 and $PtMn/SiO_2$ are associated with a change in the distribution of these interactions, possible causes of which are a substantial change of the local structure of the Mn^{II} sites or, more likely, interaction of the Mn^{II} sites with the nanoparticles.

We then performed an EXAFS analysis of $PtMn/SiO_2$ at the Pt L_{III} edge (Table 2 and Figure 2B) to confront the MTD analysis with experimental data. As can be seen from Table 2, the best fit could be obtained by inclusion of a Pt−Pt and Pt−Mn path supporting direct PtMn interaction. The removal of the Pt−Mn path led to worse fits (Figure S32 and Table S5). The total CN is significantly lower than what is observed for Pt/SiO_2 (Figures S31 and S33 and Tables S4 and S6), which is consistent with the presence of smaller particles for $PtMn/SiO_2$ compared to Pt/SiO_2 (compare STEM). Notably, CNs of around 5.9 (Pt−Pt) and 1.5 (Pt−Mn) indicate a nearest neighbor ratio of 4:1 (Pt−Mn) in $PtMn/SiO_2$ which is much lower than what is expected for both Pt_2Mn (random alloy, face centered cubic (FCC) structure, 1:1 (Pt−Mn) ratio) and Pt_3Mn (ordered, FCC structure, 2:1 (Pt−Mn) ratio), indicating spatial separation of Pt and Mn inside the particles just as the MTD calculation suggests.[46] This is also supported by calculating the Cowley parameter for the Pt_2Mn nanoparticles ($\alpha_{PtMn/SiO_2} = 0.39$; $−0.5 \leq \alpha \leq +1$ for a 2:1 bulk alloy), where a value of −0.5 indicates 100% homogeneous mixing of a binary system and +1 total segregation with no interaction of the two components (see the Supporting Information for details on the calculation of the parameter).[47] It should be noted that due to a high surface to volume ratio in nanoparticles, the expected α value should generally be lower than what would be expected for its corresponding bulk material. To further understand these materials and gather information about the structure of the Pt_2Mn nanoparticles, we then performed a refinement of the nanoparticle structure in vacuum using MTD at the DFT level to evaluate the interaction of Pt and Mn in these bimetallic systems. A 2:1 Pt−Mn particle ($Pt_{24}Mn_{14}$, ø ∼ 0.9 nm) with a random arrangement of atoms—chosen based on the combined STEM, EA and LCF XANES results indicating 1 nm sized Pt_2Mn nanoparticles—was first equilibrated for 2 ps in vacuum at 873 K in the canonical (NVT) ensemble. The particle structure was then studied using Pt and Mn CNs (CN^{MnMn}, CN^{MnPt}, and CN^{PtPt}; see the computational details for the definition of CNs used for the MTD simulation) as collective variables, in order to ensure the efficient exploration of the possible global conformation (alloy, core−shell, etc.). During

also performed an *in situ* electron paramagnetic resonance (EPR) study of the reduction of $Pt^{II}\_Mn^{II}/SiO_2$ which indicates 34% loss of EPR active Mn species—attributed to the reduction of Mn^{II} to Mn^0—in good agreement with the changes observed in XANES and the corresponding LCF (Figure S39). Additionally, following the CO IR and XANES results, we were interested to investigate whether there was a direct interaction between the PtMn nanoparticles and the remaining Mn^{II} sites at the support surface. EPR shows a clear difference between the Mn^{II}/SiO_2 and $PtMn/SiO_2$ materials (see the Supporting Information for more detail and additional spectra), namely, a strong line broadening of the bimetallic material is observed at low temperatures. At the expected mean distance between Mn^{II} centers on the order of 1 nm,

Table 1. Presentation of LCF and EA Results and Deduced Composition of the PtMn Nanoparticles in $PtMn/SiO_2$

element	% reduced (XANES)	EA [mmol M/g_{SiO_2}]	M in NP [mmol/g_{SiO_2}]	average Pt/Mn ratio in particles	single site M on support surface [mmol/g_{SiO_2}]	single site M density [M/nm^2]
Mn	30%	0.244	0.073	1	0.171	0.51
Pt	100%	0.152	0.152	2	0	0

Table 2. EXAFS Fit Parameters at the Pt L_{III} Edge for Pt/SiO$_2$ and PtMn/SiO$_2$[a]

material	path	nearest neighbors	r [Å]	σ^2 [Å^2]	ΔE_0 [eV]	R factor
Pt/SiO$_2$	Pt–Pt	9.6 ± 0.3	2.73 ± 0.002	0.006 ± 0.001	7.3 ± 0.3	0.002
PtMn/SiO$_2$	Pt–Mn	1.5 ± 0.5	2.68 ± 0.01	0.010 ± 0.003	3.7 ± 0.7	0.007
	Pt–Pt	5.9 ± 0.8	2.66 ± 0.004	0.009 ± 0.001		

[a]Notation: r, scattering path length between absorber and scatterer. σ^2, mean square relative displacement (Debye−Waller-factor). ΔE_0, internal energy alignment.

the first 12 ps of the simulation, the Mn−Mn MTD CN increased from 4 to 6 approximately (Figure S40) while the average distance of Mn atoms to the center of mass decreased by 1 Å (Figure 3A-right). Pt and Mn rapidly segregate within the NP, leading to the formation of a core−shell like structure with Mn preferentially in the core of the particle (Figure 3A-left). The reconstructed free-energy surface bears two minima: a global minimum corresponding to the core−shell structure and a second minima approximately 9 kcal mol^{-1} per Pt$_2$Mn unit uphill, corresponding to a more alloyed structure, with small manganese clusters (Figure 3C-middle). This first simulation on a simple model already clearly indicates that the formation of a homogeneous PtMn alloy is not favored. The low affinity of Mn for Pt leads to segregation within the Pt$_2$Mn nanoparticle.

The structure obtained from the simple model proved furthermore useful to rationalize the experimental FTIR results of adsorbed CO at the surface of the PtMn/SiO$_2$ material. The previously obtained core−shell Pt$_2$Mn nanoparticle was covered with 11 CO molecules, and its configurational space was explored using MTD. In addition to the C to Pt and C to Mn CNs (CN^{CMn} and CN^{CPt}) used to explore the coordination modes of CO, the Pt and Mn CNs (CN^{MnMn}, CN^{MnPt}, and CN^{PtPt}) were used to explore possible reorganization of the nanoparticle (Figure S45). IR spectra were computed for a series of representative structures selected along the MTD run (see Supporting Information for the selected structures and all simulated spectra). The best agreement to the experimental spectrum was obtained in the case of a distorted core−shell structure. In this structure CO is mainly coordinated to Pt but some Mn atoms are accessible at the nanoparticle surface (Figure 3B-left). The simulated spectrum shows three main bands at 1893, 2047, and 2085 cm^{-1} (Figure 3B-right, black line). The lowest vibrational band at 1893 cm^{-1} corresponds to the stretching frequency of μ^2-bridging carbonyls on adjacent Pt atoms and the band at 2085 cm^{-1} is related to CO adsorbed on a single platinum site. The other calculated redshifted band at 2047 cm^{-1} is assigned to Pt carbonyls that interact weakly with neighboring Mn (Figure 3B-right, blue line), which is consistent with previous reports that proximity to other metallic sites causes a redshift of the stretching frequency of CO adsorbed on Pt.[48] To further validate this assignment, we performed harmonic frequency calculations on the [Mn−Pt−CO] fragment for various ∠Mn−Pt−C angles (see the computational details and see the Supporting Information, Figure S53). While the ∠Mn−Pt−C angle decreases, the interaction with Mn increases, as evidenced by a decreasing ∠Pt−C−O angle. In turn, the stretching frequency decreases. The results from the CO IR simulation clarify the origin of the experimentally observed vibrational features of the PtMn/SiO$_2$ material, namely, the feature at 2026 cm^{-1} is best assigned to CO adsorbed on Pt with Mn adjacent sites. This indicates that a portion of the

interface between the Pt and Mn phases should be accessible to CO molecules.

However, while the Mn and Pt separation is qualitatively reproduced by the MTD exploration of the NP in vacuum, the Pt to Mn CNs obtained (Pt−Mn: ∼3.5; Pt−Pt: ∼4) are significantly too high compared to the ones obtained from the EXAFS analysis while the Pt−Pt CNs and Cowley parameter are too low. This indicates that the spatial segregation between the Pt and Mn phases expected in vacuum is lower compared to the one observed experimentally on the silica-supported system containing residual Mn^{II} sites. We therefore further refined the structure obtained from the MTD calculations to possibly unify the computational and experimental structural analysis.

As recently demonstrated by MTD calculations for a SOMC-derived PtGa system, a strong effect of the support on the nanoparticle structure can be expected.[35] We thus investigated the role of the oxide support by building a more complex model placing the core−shell Pt$_2$Mn particle—identified as the energetic ground state in the preceding calculation in vacuum—at the surface of an amorphous dehydroxylated silica support[49] bearing 5 Mn^{II} sites (see Supporting Information for details on the construction of this oxide model). Along the simulation, the Mn−O MTD CN increases steadily at the expense of the Mn−Mn and Mn−Pt CNs, which tend to decrease along the simulation, suggesting a strong affinity of Mn^0 for the oxide support (Figures 3C-right and S54). This is further supported by the distribution of the positions along the z axis: most of the manganese is located between the Pt and the oxide support (Figures 3C-left and S57). Additionally, the Mn^0 located on the outer part of the particle interacts not only with the silica support (increased Mn−O CN number) but also with the Mn^{II} sites at the interface between particle and support.

Toward the end of the simulation, CNs as low as ∼2.8 for Pt−Mn (N^{Mn-Pt} = 3.5) and as high as ∼5.0 for Pt−Pt are found (Figure 3C-middle). This corresponds to a higher spatial separation of Pt and Mn phases compared to the vacuum NP, as further illustrated by the evolution of the Cowley parameter (Figure 3C-right), which increases over the course of the simulation—from −0.09 to +0.04—indicating an increased segregation between Pt and Mn associated with an evolution toward a structure with Mn at the surface of the Pt particle, interacting with the support surface. The interactions with the support play a critical role in explaining the segregated structure of the Pt$_2$Mn nanoparticles. The CNs obtained from the MTD run on the more complex model are in much better agreement with the ones obtained from EXAFS analysis (N^{Pt-Mn} = 1.5 ± 0.5; N^{Pt-Pt} = 5.9 ± 0.8, α > 0).

Overall, experimental characterizations and the MTD simulation are pointing toward a highly segregated structure for the Pt$_2$Mn NPs supported on Mn^{II}-decorated SiO$_2$ with Pt on top, supported on a reduced Mn^0 phase interacting with the Mn^{II} sites and oxygen on the surface (Figure 1A). This
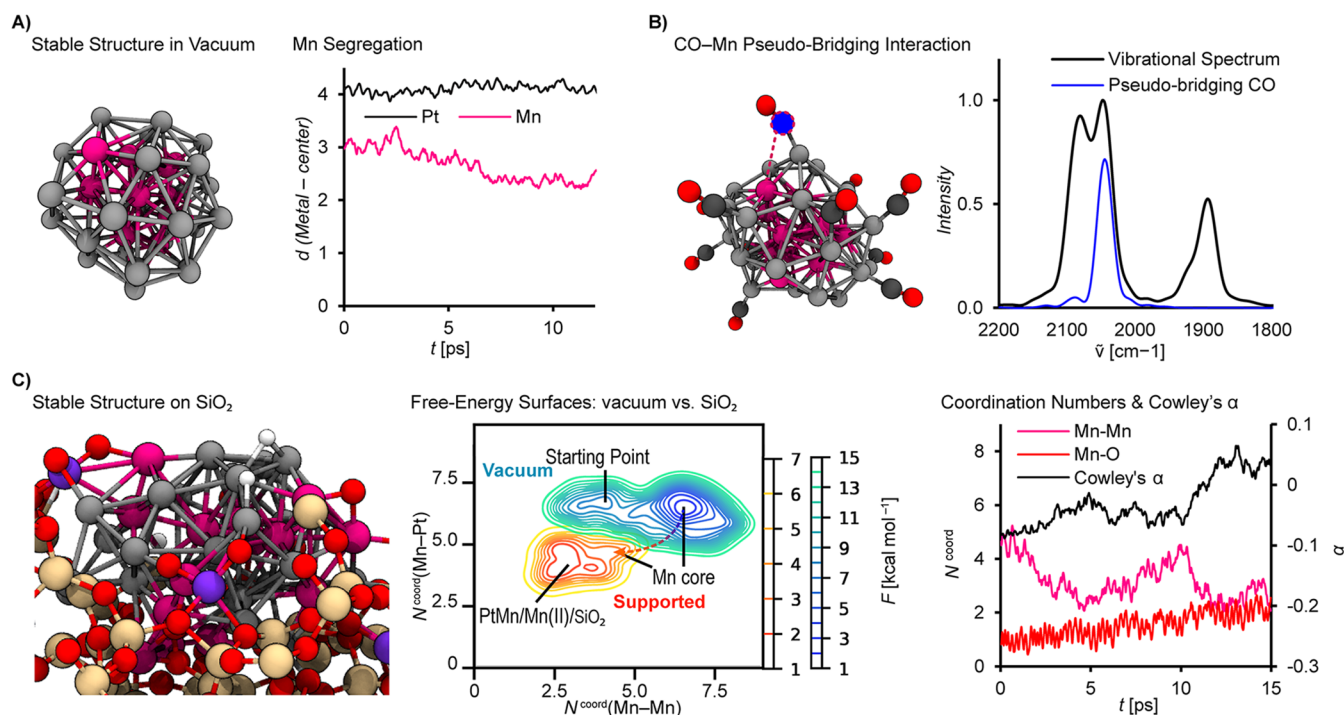
Figure 3. (A) Nanoparticle in vacuum. Left—Snapshot of the structure of the $Pt_{24}Mn_{14}$ particle in vacuum around the energy minimum, Mn in pink, Pt in gray. Right—Average distance to the center of the particle for each element, highlighting Mn segregation. (B) Simulated CO adsorption vibrations. Left—Starting structure of the simulation of the production run of the vibrational spectrum. A CO molecule and its interaction with a neighboring Mn atom is highlighted in blue. Right—Simulated vibrational spectrum (black line) and contribution of the highlighted pseudo-bridging CO to the overall spectrum (blue line), identifying the origin of the vibrational feature at 2026 cm^{-1} in the experimental CO FTIR spectrum. (C) Nanoparticle-oxide interaction. Left—Snapshot representative of the free-energy minimum. Mn^{II} single sites are in purple, Si beige, O in red. Middle—Free-energy surfaces projected along the Mn−Pt and Mn−Mn CNs, for the particle in vacuum and on the support, indicating decreased Mn−Pt and Pt−Pt interaction for the particle at the support surface. Right—Mn−Mn, Mn−O CNs and Cowley parameter highlighting a segregation of Mn due to its interaction with the surface. The definition of CNs, additional free-energy surfaces, free-energy profiles, as well as videos of MTD simulations are available as Supporting Information.

Table 3. Catalytic Parameters for PDH Catalytic Tests of Mn^{II}/SiO_2, Pt/SiO_2, $PtMn/SiO_2$, and $Pt(0.05)Mn/SiO_2$

material	feed[a]	time [h]	T [°C]	conv. [%]	select. [%]	WHSV[b] [$g_{C_3H_8}/g_M$ h]	productivity[b] [$g_{C_3H_6}/g_M$ h]	k_d [h^{-1}]	wt % M
Mn^{II}/SiO_2		0.1		1.7	56.6	4839	44.4	0.031	1.37 Mn
		2		1.6	55.7		41.8		
Pt/SiO_2		0.1		17.2	81.5	834	110	1.464	3.96 Pt
		2		1.1	77.8		7		
$PtMn/SiO_2$	1:4 C_3H_8/Ar	0.1		39.9	96.1	2246	822	0.018	2.97 Pt, 1.34 Mn
		60	550	18.1	97.3		373		
$PtMn/SiO_2$		0.1		40.7	92.5	1160	416	0.011	2.97 Pt, 1.34 Mn
		60		26.6	99.1		272		
$Pt(0.05)Mn/SiO_2$		0.1		22.2	98.4	27369	5705	0.032	0.052 Pt, 1.38 Mn
		60		4.1	89.8		1054		
$Pt(0.05)Mn/SiO_2$	1:1:3 C_3H_8/H_2/Ar	0.1		17.8	97.3	27369	4523	0.003	0.052 Pt, 1.38 Mn
		160		11.2	96.4		2846		

[a]10 mL/min C_3H_8, 40 mL/min Ar or 10 mL/min C_3H_8, 10 mL/min H_2, 30 mL/min Ar. [b]M in g_M is Mn for Mn^{II}/SiO_2 and Pt otherwise.

structure is in significant contrast to the ones currently proposed for PtMn systems for which homogeneous PtMn alloyed phases were suggested. The effect of the Mn-promoter also sharply contrasts with the currently reported PtGa system, which features homogeneously alloyed PtGa nanoparticles.[26,27,35] Finally, the strong affinity of the Mn for the support surface and the residual Mn^{II} sites suggests that Mn plays a key role as an "anchor", which interacts strongly with both the support and the inner, Pt-rich part of the segregated Pt_2Mn nanoparticles—consistent with the changes in EPR of

$PtMn/SiO_2$ compared to Mn^{II}/SiO_2—which could play an important role in sintering/deactivation prevention during catalytic PDH conditions.

We then evaluated the catalytic performance of this material in PDH, exploring several conditions. The catalytic results are summarized in Table 3 (see the Supporting Information for more detail). The $PtMn/SiO_2$ material (3 wt % Pt, 1.3 wt % Mn) shows both very good productivity (initial: 822 $g_{C_3H_6}/g_{Pt}$ h) and stability (low k_d of 0.018 h^{-1}) over 60 h on stream
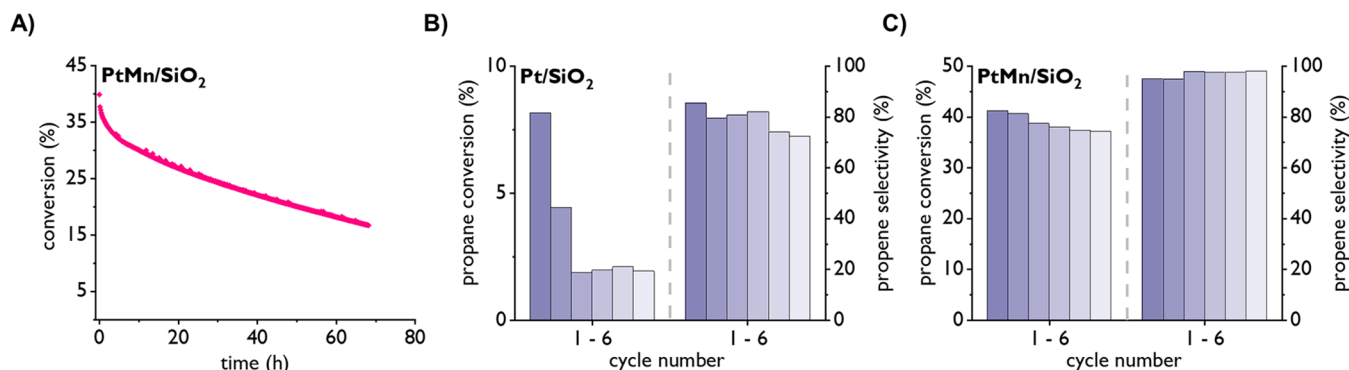
Figure 4. (A) Conversion levels of PtMn/SiO$_2$ (WHSV of 2246 h^{-1}) over 70 h on stream, indicating good stability of the material. (B,C) Performance (left: conversion and right: propene selectivity) of Pt/SiO$_2$ and PtMn/SiO$_2$ during 6 fast, consecutive regeneration cycles, indicating considerably increased robustness of the bimetallic material compared to the monometallic counterpart.

(Figure 4A). These values greatly exceed what is obtained with pure Pt supported on SiO$_2$ (initial: 105 g$_{C_3H_6}$/g$_{Pt}$ h, k_d of 1.464 h^{-1}) and surpass what is observed for PtZn/SiO$_2$ (initial: 703 g$_{C_3H_6}$/g$_{Pt}$ h; k_d of 0.027 h^{-1}) and PtGa/SiO$_2$ (initial: 722 g$_{C_3H_6}$/g$_{Pt}$ h, k_d of 0.04 h^{-1}) prepared *via* a similar approach as well as any other PtMn system reported in literature.[6,16,26,27] It is noteworthy that a much higher initial productivity is obtained upon decreasing the Pt loading to 0.05 wt %.

While inherently difficult to characterize due to the very low Pt loading, this material—Pt(0.05)Mn/SiO$_2$—shows initial productivity levels that are among the highest reported to date.[12] In the presence of H$_2$ (1:1:3 C$_3$H$_8$/H$_2$/Ar)—a common condition in PDH catalysis—such a catalyst still shows comparable productivity (4523 g$_{C_3H_6}$/g$_{Pt}$ h) and additionally outstanding stability (k_d of 0.003 h^{-1}) over 160 h on stream, highlighting the outstanding performance of such SOMC-derived PtMn catalysts (Figure S65). It is noteworthy that the PSD almost does not change for the PtMn/SiO$_2$ (+0.2 nm after 66 h) and Pt(0.05)Mn/SiO$_2$ (+0.1 nm after 48 h) materials during PDH conditions, which is in contrast to what is observed for monometallic Pt/SiO$_2$ (+0.5 nm after 8.7 h) (see Supporting Information for detail, Figures S3, S7, and S10). These observations verify what we proposed in that Mn plays an important role for sintering prevention. While both investigated materials also contain a small fraction of Pt single sites (Figures S5 and S9), they only make up a very minor fraction of overall surface Pt and therefore very likely do not contribute significantly to the catalytic activity in these samples.

With these results in hand, we evaluated the stability of PtMn/SiO$_2$ upon fast cycling by monitoring the evolution of the catalysts by STEM energy-dispersive X-ray spectroscopy (STEM-EDXS). For this purpose, we applied repeated cycles of C$_3$H$_8$, O$_2$/Ar, and H$_2$ flow at high temperature designed to test the robustness of the PtMn/SiO$_2$ system toward repeated short regeneration phases, which are also applied in industrial settings.[17] We tested both Pt/SiO$_2$ and PtMn/SiO$_2$ under short deactivation phases followed by short oxidation and reduction treatments (Table 4 and Figure 4B,C, see Supporting Information for detail).

PtMn/SiO$_2$ shows an outstanding performance with little deactivation over 6 cycles, approaching a very high level of conversion of around 37%, which is just below equilibrium

conversion (around 40%, Figure 4C) and a very high selectivity of 98%. In comparison, Pt/SiO$_2$ performs poorly under such regeneration conditions—2% conversion after 6 cycles and 72% propene selectivity—with deactivation to almost background level (SiC: 1.4% propane conversion, Figure S59) and low selectivity for propene over 6 cycles (Figure 4B).

Comparing the two materials after regeneration shows that the average particle size in Pt/SiO$_2$ grows quite significantly,

Table 4. Regeneration Data for the Fast Regeneration Cycles of Pt/SiO$_2$ and PtMn/SiO$_2$[a]

material	regeneration cycle	conv. [%][b]	select. [%][b]	PSD[c]
Pt/SiO$_2$	1	8.2	79.4	2.0 ± 0.8
	6	1.9	77.3	2.6 ± 0.8
PtMn/SiO$_2$	1	41.2	95.0	1.0 ± 0.3
	6	37.0	98.0	1.2 ± 0.8

[a]PDH cycles of 20 min at 550 °C (WHSV of 1160 h^{-1} (PtMn/SiO$_2$) and 857 h^{-1} (Pt/SiO$_2$)) with flow of 5% O$_2$/Ar at 500 °C for 20 min and 100% H$_2$ at 550 °C for 20 min in deactivation phases. [b]Average of 20 min (3 data points). [c]Before 1st cycle and after 6th cycle.

that is, by 0.6 nm in diameter, albeit with unchanged size homogeneity in contrast to PtMn/SiO$_2$ where almost no particle growth is observed (0.2 nm), while the size homogeneity decreases. The PSD for PtMn/SiO$_2$ after the fast cycles is best modelled by a lognormal distribution (see Supporting Information Figures S4 and S8). A large majority of very small (below 1 nm) particles are observable, while a small minority of larger particles exist. This behavior can again be attributed to a strong interaction of the Mn in the nanoparticles with remaining Mn^{II} sites at the support surface consistent with what has been found in CO IR and the MTD study, most likely contributing to reduced particle sintering during the regeneration cycles.

Notably, EXAFS fitting at the Pt L$_{III}$ edge after conducting a regeneration cycle on the PtMn/SiO$_2$ material results in an almost identical fit when compared to the pristine material, with almost unchanged CNs (see Supporting Information for detail, Figure S35 and Table S8). This result supports minor particle growth and insignificant structural change during such harsh regeneration conditions, in line with the STEM study. The TEM results in combination with the data of the short regeneration cycles for PtMn/SiO$_2$ point toward a stabilization of the conversion at high levels with very high propene

selectivity and a very good sintering prevention of the PtMn particles on the support surface, underlining the robustness of the material toward repeated treatment under harsh regeneration conditions, making it an interesting alternative candidate for industrial PDH application. This is in contrast to what is observed for Pt/SiO$_2$, which is not robust toward regeneration with fast deactivation and more severe particle growth.

3. CONCLUSIONS

In this work, we describe the synthesis and the detailed characterization of a silica-supported PtMn material—PtMn/SiO$_2$—which shows a high productivity, selectivity, and robustness in the PDH reaction. Thanks to its tailored synthesis *via* an SOMC/TMP approach and the multi-technique characterization approach, including CO IR, STEM, XAS, and EPR, further supported by MTD calculations, we could show that this material consists of homogeneously distributed and size uniform Pt$_2$Mn nano-particles, supported on a Mn^{II}-decorated (70% of the overall Mn) silica support with noteworthy and unexpected structure. Combined EXAFS analysis and MTD calculations identify significant spatial segregation of Pt and Mn, with Pt mostly forming the inner part of the particles, while most of the Mn^0 accumulates at the interface between Pt and the silica support, forming a half shell around the Pt core. Despite the segregated nature, which is viewed as detrimental for a highly performing PDH catalyst, PtMn/SiO$_2$ (3 wt % Pt, 1.3 wt % Mn) displays high productivity. Furthermore, PtMn/SiO$_2$ shows great robustness toward consecutive regeneration cycles, which is attributed to reduced sintering under such harsh conditions, compared to the monometallic Pt counterpart. This robustness is attributed to the strong interaction of the Mn^0 at the surface of the nanoparticles with the Mn^{II}-decorated silica support. Notably, a material with a similar Mn content but much lower Pt loading of only 0.05 wt % revealed outstanding performance per g$_{Pt}$, ranging among the highest reported productivities (4523 g$_{C_3H_6}$/g$_{Pt}$ h) to date, with almost no deactivation over 160 h on stream when operating under a partial pressure of H$_2$. Overall, we have demonstrated that the combination of SOMC and state-of-the-art spectroscopy refined with MTD at the DFT level provide a powerful tool to develop well-defined bimetallic materials and to understand their structure with molecular-level precision, here revealing an unexpectedly segregated structure for a highly performing and robust PDH catalyst. These findings indicate that site isolation may not be a prerequisite for high performance in alkane dehydrogenation catalysts. We are currently further exploring related systems.

■ ASSOCIATED CONTENT

ⓢ Supporting Information

The Supporting Information is available free of charge at https://pubs.acs.org/doi/10.1021/jacs.2c05618.

> Detailed experimental procedures, general considerations, microscopy data, spectroscopy data of all methods, and associated data (PDF)
> Videos of MTD simulations (ZIP)

■ AUTHOR INFORMATION

Corresponding Authors

Pierre-Adrien Payard − *Université de Lyon, Université Claude Bernard Lyon I, CNRS, INSA, CPE, UMR 5246, ICBMS, F-69622 Villeurbanne Cedex, France;* ⓞ orcid.org/0000-0001-5661-6128; Email: pierre-adrien.payard@univ-lyon1.fr

Christophe Copéret − *Department of Chemistry and Applied Biosciences, ETH Zürich, CH-8093 Zürich, Switzerland;* ⓞ orcid.org/0000-0001-9660-3890; Email: ccoperet@ethz.ch

Authors

Lukas Rochlitz − *Department of Chemistry and Applied Biosciences, ETH Zürich, CH-8093 Zürich, Switzerland*

Quentin Pessemesse − *Department of Chemistry and Applied Biosciences, ETH Zürich, CH-8093 Zürich, Switzerland; Université de Lyon, Université Claude Bernard Lyon I, CNRS, INSA, CPE, UMR 5246, ICBMS, F-69622 Villeurbanne Cedex, France*

Jörg W. A. Fischer − *Department of Chemistry and Applied Biosciences, ETH Zürich, CH-8093 Zürich, Switzerland*

Daniel Klose − *Department of Chemistry and Applied Biosciences, ETH Zürich, CH-8093 Zürich, Switzerland;* ⓞ orcid.org/0000-0002-3597-0889

Adam H. Clark − *Paul Scherrer Institut, CH-5232 Villigen, Switzerland;* ⓞ orcid.org/0000-0002-5478-9639

Milivoj Plodinec − *Department of Chemistry and Applied Biosciences, ETH Zürich, CH-8093 Zürich, Switzerland*

Gunnar Jeschke − *Department of Chemistry and Applied Biosciences, ETH Zürich, CH-8093 Zürich, Switzerland;* ⓞ orcid.org/0000-0001-6853-8585

Complete contact information is available at:
https://pubs.acs.org/10.1021/jacs.2c05618

Author Contributions

The manuscript was written through contributions of all authors. All authors have given approval to the final version of the manuscript.

Notes

The authors declare no competing financial interest.

■ ACKNOWLEDGMENTS

■ REFERENCES

(1) Sattler, J. J. H. B.; Ruiz-Martinez, J.; Santillan-Jimenez, E.; Weckhuysen, B. M. Catalytic Dehydrogenation of Light Alkanes on Metals and Metal Oxides. *Chem. Rev.* **2014**, *114*, 10613−10653.

(2) Marsh, M.; Wery, J. *Filling the Propylene Gap—Shaping the Future with On-Purpose Technologies*; Honeywell UOP, 2019.

(3) Nawaz, Z. Light Alkane Dehydrogenation to Light Olefin Technologies: A Comprehensive Review. *Rev. Chem. Eng.* 2015, 31, 413−436.

(4) Chen, S.; Chang, X.; Sun, G.; Zhang, T.; Xu, Y.; Wang, Y.; Pei, C.; Gong, J. Propane Dehydrogenation: Catalyst Development, New Chemistry, and Emerging Technologies. *Chem. Soc. Rev.* 2021, 50, 3315−3354.

(5) Pham, H. N.; Sattler, J. J. H. B.; Weckhuysen, B. M.; Datye, A. K. Role of Sn in the Regeneration of Pt/γ-Al2O3 Light Alkane Dehydrogenation Catalysts. *ACS Catal.* 2016, 6, 2257−2264.

(6) Rochlitz, L.; Searles, K.; Alfke, J.; Zemlyanov, D.; Safonova, O. V.; Copéret, C. Silica-Supported, Narrowly Distributed, Subnanometric Pt-Zn Particles from Single Sites with High Propane Dehydrogenation Performance. *Chem. Sci.* 2020, 11, 1549−1555.

(7) Camacho-Bunquin, J.; Ferrandon, M. S.; Sohn, H.; Kropf, A. J.; Yang, C.; Wen, J.; Hackler, R. A.; Liu, C.; Celik, G.; Marshall, C. L.; Stair, P. C.; Delferro, M. Atomically Precise Strategy to a PtZn Alloy Nanocluster Catalyst for the Deep Dehydrogenation of n-Butane to 1,3-Butadiene. *ACS Catal.* 2018, 8, 10058−10063.

(8) Cybulskis, V. J.; Bukowski, B. C.; Tseng, H.-T.; Gallagher, J. R.; Wu, Z.; Wegener, E.; Kropf, A. J.; Ravel, B.; Ribeiro, F. H.; Greeley, J.; Miller, J. T. Zinc Promotion of Platinum for Catalytic Light Alkane Dehydrogenation: Insights into Geometric and Electronic Effects. *ACS Catal.* 2017, 7, 4173−4181.

(9) de Miguel, S. R.; Jablonski, E. L.; Castro, A. A.; Scelza, O. A. Highly Selective and Stable Multimetallic Catalysts for Propane Dehydrogenation. *J. Chem. Technol. Biotechnol.* 2000, 75, 596−600.

(10) Qi, L.; Babucci, M.; Zhang, Y.; Lund, A.; Liu, L.; Li, J.; Chen, Y.; Hoffman, A. S.; Bare, S. R.; Han, Y.; Gates, B. C.; Bell, A. T. Propane Dehydrogenation Catalyzed by Isolated Pt Atoms in ≡SiOZn-OH Nests in Dealuminated Zeolite Beta. *J. Am. Chem. Soc.* 2021, 143, 21364−21378.

(11) Fan, X.; Li, J.; Zhao, Z.; Wei, Y.; Liu, J.; Duan, A.; Jiang, G. Dehydrogenation of Propane over PtSn/SBA-15 Catalysts: Effect of the Amount of Metal Loading and State. *RSC Adv.* 2015, 5, 28305−28315.

(12) Chen, S.; Zhao, Z.-J.; Mu, R.; Chang, X.; Luo, J.; Purdy, S. C.; Kropf, A. J.; Sun, G.; Pei, C.; Miller, J. T.; Zhou, X.; Vovk, E.; Yang, Y.; Gong, J. Propane Dehydrogenation on Single-Site [PtZn4] Intermetallic Catalysts. *Chem* 2021, 7, 387−405.

(13) Zhang, Y.; Qi, L.; Leonhardt, B.; Bell, A. T. Mechanism and Kinetics of n-Butane Dehydrogenation to 1,3-Butadiene Catalyzed by Isolated Pt Sites Grafted onto ≡SiOZn-OH Nests in Dealuminated Zeolite Beta. *ACS Catal.* 2022, 12, 3333−3345.

(14) Byron, C.; Bai, S.; Celik, G.; Ferrandon, M. S.; Liu, C.; Ni, C.; Mehdad, A.; Delferro, M.; Lobo, R. F.; Teplyakov, A. V. Role of Boron in Enhancing the Catalytic Performance of Supported Platinum Catalysts for the Nonoxidative Dehydrogenation of N-Butane. *ACS Catal.* 2020, 10, 1500−1510.

(15) Aly, M.; Fornero, E. L.; Leon-Garzon, A. R.; Galvita, V. V.; Saeys, M. Effect of Boron Promotion on Coke Formation during Propane Dehydrogenation over Pt/γ-Al2O3 Catalysts. *ACS Catal.* 2020, 10, 5208−5216.

(16) Searles, K.; Chan, K. W.; Mendes Burak, J. A.; Zemlyanov, D.; Safonova, O.; Copéret, C. Highly Productive Propane Dehydrogenation Catalyst Using Silica-Supported Ga-Pt Nanoparticles Generated from Single-Sites. *J. Am. Chem. Soc.* 2018, 140, 11674−11679.

(17) Sattler, J. J. H. B.; Gonzalez-Jimenez, I. D.; Luo, L.; Stears, B. A.; Malek, A.; Barton, D. G.; Kilos, B. A.; Kaminsky, M. P.; Verhoeven, T. W. G. M.; Koers, E. J.; Baldus, M.; Weckhuysen, B. M. Platinum-Promoted Ga/Al2O3 as Highly Active, Selective, and Stable Catalyst for the Dehydrogenation of Propane. *Angew. Chem., Int. Ed.* 2014, 53, 9251−9256.

(18) Nakaya, Y.; Xing, F.; Ham, H.; Shimizu, K. i.; Furukawa, S. Doubly Decorated Platinum-Gallium Intermetallics as Stable Catalysts for Propane Dehydrogenation. *Angew. Chem., Int. Ed.* 2021, 60, 19715−19719.

(19) Raman, N.; Wolf, M.; Heller, M.; Heene-Würl, N.; Taccardi, N.; Haumann, M.; Felfer, P.; Wasserscheid, P. GaPt Supported Catalytically Active Liquid Metal Solution Catalysis for Propane Dehydrogenation-Support Influence and Coking Studies. *ACS Catal.* 2021, 11, 13423−13433.

(20) Nakaya, Y.; Hirayama, J.; Yamazoe, S.; Shimizu, K.-i.; Furukawa, S. Single-Atom Pt in Intermetallics as an Ultrastable and Selective Catalyst for Propane Dehydrogenation. *Nat. Commun.* 2020, 11, 3−9.

(21) Li, J.; Zhang, M.; Song, Z.; Liu, S.; Wang, J.; Zhang, L. Hierarchical PtIn/Mg(Al)O Derived from Reconstructed PtIn-Hydrotalcite-like Compounds for Highly Efficient Propane Dehydrogenation. *Catalysts* 2019, 9, 767.

(22) Liu, J.; Zhou, W.; Jiang, D.; Wu, W.; Miao, C.; Wang, Y.; Ma, X. Isobutane Dehydrogenation over InPtSn/ZnAl2O4 Catalysts: Effect of Indium Promoter. *Ind. Eng. Chem. Res.* 2018, 57, 11265−11270.

(23) Liu, X.; Lang, W.-Z.; Long, L.-L.; Hu, C.-L.; Chu, L.-F.; Guo, Y.-J. Improved catalytic performance in propane dehydrogenation of PtSn/γ-Al2O3 catalysts by doping indium. *Chem. Eng. J.* 2014, 247, 183−192.

(24) Shi, L.; Deng, G.-M.; Li, W.-C.; Miao, S.; Wang, Q.-N.; Zhang, W.-P.; Lu, A.-H. Al2O3Nanosheets Rich in Pentacoordinate Al3+Ions Stabilize Pt-Sn Clusters for Propane Dehydrogenation. *Angew. Chem., Int. Ed.* 2015, 54, 13994−13998.

(25) Pretz, M. T.; Stewart, M. W. Catalytic Dehydrogenation Process. U.S. Patent 9,725,382 B2, 2016.

(26) Fan, X.; Liu, D.; Sun, X.; Yu, X.; Li, D.; Yang, Y.; Liu, H.; Diao, J.; Xie, Z.; Kong, L.; Xiao, X.; Zhao, Z. Mn-Doping Induced Changes in Pt Dispersion and PtxMny Alloying Extent on Pt/Mn-DMSN Catalyst with Enhanced Propane Dehydrogenation Stability. *J. Catal.* 2020, 389, 450−460.

(27) Wu, Z.; Bukowski, B. C.; Li, Z.; Milligan, C.; Zhou, L.; Ma, T.; Wu, Y.; Ren, Y.; Ribeiro, F. H.; Delgass, W. N.; Greeley, J.; Zhang, G.; Miller, J. T. Changes in Catalytic and Adsorptive Properties of 2 nm Pt3Mn Nanoparticles by Subsurface Atoms. *J. Am. Chem. Soc.* 2018, 140, 14870−14877.

(28) Copéret, C.; Comas-Vives, A.; Conley, M. P.; Estes, D. P.; Fedorov, A.; Mougel, V.; Nagae, H.; Núñez-Zarur, F.; Zhizhko, P. A. Surface Organometallic and Coordination Chemistry toward Single-Site Heterogeneous Catalysts: Strategies, Methods, Structures, and Activities. *Chem. Rev.* 2016, 116, 323−421.

(29) Samantaray, M. K.; Pump, E.; Bendjeriou-Sedjerari, A.; D'Elia, V.; Pelletier, J. D. A.; Guidotti, M.; Psaro, R.; Basset, J.-M. Surface Organometallic Chemistry in Heterogeneous Catalysis. *Chem. Soc. Rev.* 2018, 47, 8403−8437.

(30) Pelletier, J. D. A.; Basset, J.-M. Catalysis by Design: Well-Defined Single-Site Heterogeneous Catalysts. *Acc. Chem. Res.* 2016, 49, 664−677.

(31) Stalzer, M. M.; Delferro, M.; Marks, T. J. Supported Single-Site Organometallic Catalysts for the Synthesis of High-Performance Polyolefins. *Catal. Lett.* 2015, 145, 3−14.

(32) Fujdala, K. L.; Tilley, T. D. Design and Synthesis of Heterogeneous Catalysts: The Thermolytic Molecular Precursor Approach. *J. Catal.* 2003, 216, 265−275.

(33) Copéret, C. Single-Sites and Nanoparticles at Tailored Interfaces Prepared via Surface Organometallic Chemistry from Thermolytic Molecular Precursors. *Acc. Chem. Res.* 2019, 52, 1697−1708.

(34) Docherty, S. R.; Rochlitz, L.; Payard, P.-A.; Copéret, C. Heterogeneous Alkane Dehydrogenation Catalysts Investigated via a Surface Organometallic Chemistry Approach. *Chem. Soc. Rev.* 2021, 50, 5806−5822.

(35) Payard, P.-A.; Rochlitz, L.; Searles, K.; Foppa, L.; Leuthold, B.; Safonova, O. V.; Comas-Vives, A.; Copéret, C. Dynamics and Site Isolation: Keys to High Propane Dehydrogenation Performance of Silica-Supported PtGa Nanoparticles. *JACS Au* 2021, 1, 1445−1458.

(36) Searles, K.; Siddiqi, G.; Safonova, O. V.; Copéret, C. Silica-Supported Isolated Gallium Sites as Highly Active, Selective and

Stable Propane Dehydrogenation Catalysts. *Chem. Sci.* **2017**, *8*, 2661−2666.

(37) Rochlitz, L.; Searles, K.; Nater, D. F.; Docherty, S. R.; Gioffrè, D.; Copéret, C. A Molecular Analogue of the C−H Activation Intermediate of the Silica-Supported Ga(III) Single-Site Propane Dehydrogenation Catalyst: Structure and XANES Signature. *Helv. Chim. Acta* **2021**, *104*, No. e2100078.

(38) Phadke, N. M.; Mansoor, E.; Bondil, M.; Head-Gordon, M.; Bell, A. T. Mechanism and Kinetics of Propane Dehydrogenation and Cracking over Ga/H-MFI Prepared via Vapor-Phase Exchange of H-MFI with GaCl3. *J. Am. Chem. Soc.* **2019**, *141*, 1614−1627.

(39) Ghaffari, B.; Mendes-Burak, J.; Chan, K. W.; Copéret, C. Silica-Supported Mn[II] Sites as Efficient Catalysts for Carbonyl Hydroboration, Hydrosilylation, and Transesterification. *Chem.—Eur. J.* **2019**, *25*, 13869−13873.

(40) Laurent, P.; Veyre, L.; Thieuleux, C.; Donet, S.; Copéret, C. From well-defined Pt(ii) surface species to the controlled growth of silica supported Pt nanoparticles. *Dalton Trans.* **2013**, *42*, 238−248.

(41) Ruddy, D. A.; Jarupatrakorn, J.; Rioux, R. M.; Miller, J. T.; McMurdo, M. J.; McBee, J. L.; Tupper, K. A.; Tilley, T. D. Site-Isolated Pt-SBA15 Materials from Tris(tert-butoxy)siloxy Complexes of Pt(II) and Pt(IV). *Chem. Mater.* **2008**, *20*, 6517−6527.

(42) Peters, S.; Peredkov, S.; Neeb, M.; Eberhardt, W.; Al-Hada, M. Size-Dependent XPS Spectra of Small Supported Au-Clusters. *Surf. Sci.* **2013**, *608*, 129−134.

(43) Lee, Y.-S.; Lim, K.-Y.; Chung, Y.-D.; Whang, C.-N.; Jeon, Y. XPS Core-Level Shifts and XANES Studies of Cu-Pt and Co-Pt Alloys. *Surf. Interface Anal.* **2000**, *30*, 475−478.

(44) Lei, Y.; Jelic, J.; Nitsche, L. C.; Meyer, R.; Miller, J. Effect of Particle Size and Adsorbates on the L3, L2 and L1 X-Ray Absorption near Edge Structure of Supported Pt Nanoparticles. *Top. Catal.* **2011**, *54*, 334−348.

(45) Maryasov, A. G.; Bowman, M. K.; Tsvetkov, Y. D. Dipole-Dipole Interactions of High-Spin Paramagnetic Centers in Disordered Systems. *Appl. Magn. Reson.* **2006**, *30*, 683−702.

(46) Buschow, K. H. J.; van Engen, P. G.; Jongebreur, R. Magneto-Optical Properties of Metallic Ferromagnetic Materials. *J. Magn. Magn. Mater.* **1983**, *38*, 1−22.

(47) Frenkel, A. I.; Wang, Q.; Sanchez, S. I.; Small, M. W.; Nuzzo, R. G. Short Range Order in Bimetallic Nanoalloys: An Extended X-Ray Absorption Fine Structure Study. *J. Chem. Phys.* **2013**, *138*, 064202.

(48) Aleksandrov, H. A.; Neyman, K. M.; Hadjiivanov, K. I.; Vayssilov, G. N. Can the State of Platinum Species Be Unambiguously Determined by the Stretching Frequency of an Adsorbed CO Probe Molecule? *Phys. Chem. Chem. Phys.* **2016**, *18*, 22108−22121.

(49) Comas-Vives, A. Amorphous SiO2 Surface Models: Energetics of the Dehydroxylation Process, Strain, Ab Initio Atomistic Thermodynamics and IR Spectroscopic Signatures. *Phys. Chem. Chem. Phys.* **2016**, *18*, 7475−7482.

🔲 Recommended by ACS